L-subshell ionization of Bi, Au, and Yb induced by F ions at intermediate velocities

Y. P. Singh, D. Mitra, Lokesh C. Tribedi, and P. N. Tandon
Tata Institute of Fundamental Research, Homi Bhabha Road, Colaba, Mumbai 400 005, India
(Received 22 June 2000; revised manuscript received 28 July 2000; published 12 December 2000)

We have measured the absolute cross sections for the *L*-subshell ionization for Yb, Au, and Bi induced by intermediate and low-energy F ions. A comparative study of the different methods of extracting the vacancy production cross sections from the *L* x-ray line intensities is presented. The measured cross sections are compared with the available theoretical calculations based on the perturbed stationary state (PSS) approximation including the effects due to the increased binding energy, Coulomb (C) deflection, energy (E) loss, and the relativistic (R) wave function (ECPSSR). In the case of Yb and Au targets, the ratio of the subshell ionization cross section for L_1 to that for L_2 is found to be larger than 1.0 contrary to theoretical predictions, whereas the ratio is less than 1.0 for Bi, as expected. Similar ratios for the L_2 to L_3 subshells are, however, in agreement with the theoretical predictions for all three targets. These observations can be understood in terms of the multiple vacancies in the outer shells and their effect on the fluorescence yields and Coster-Kronig transitions. In the case of L_1 ionization, the ECPSSR calculations are found to fall much below the experimental data for Yb and Au, and a part of the deviation is understood to be due to the existence of multiple vacancies in the outer shells and the interplay between the Coster-Kronig and radiative transition probability. Quantitative estimates on the enhancement in the effective fluorescence yields of the L_1 subshell are also provided for all three targets.

DOI: 10.1103/PhysRevA.63.012713 PACS number(s): 34.50.Fa

I. INTRODUCTION

The ionization of the inner atomic shells by highly charged particles is an important field of atomic collision physics from both a theoretical point of view and applications. For highly asymmetric collisions (i.e., $Z_1/Z_2 \ll 1$, where Z_1 and Z_2 represent the atomic numbers of the projectile and the target, respectively), the direct Coulomb ionization mechanism is a dominating process [1,2]. Among the various inner shells, the *L* subshells in particular provide a suitable testing ground for the theoretical models on direct ionization. They consist of three subshells having somewhat different properties. The L_2 and L_3 wave functions are similar with widely different binding energies (in heavier atoms) and, in contrast, the L_1 and L_2 subshells have wave functions of different shapes but with similar binding energies. Thus various aspects of the ionization mechanism can be closely examined by studying *L*-subshell ionization for different target projectile combination at different impact energies. These studies therefore provide a crucial test for the various models of inner-shell ionization, e.g., the plane-wave Born approximation (PWBA) [3], the semiclassical approximation (SCA) [4], and the perturbed stationary state (PSS) approach including correction factors for the projectile energy loss (E), Coulomb (C) deflection, and the relativistic motion (R) of the orbital electrons (ECPSSR) [5]. Several measurements have been reported in the past, especially using light projectiles such as H and He, and it is now clear that it will be necessary to go beyond the first-order perturbation treatment [6–8]. Semiclassical close-coupling calculations by Shingal *et al.* [8] explained quite well the energy dependence of the $L\gamma_{2,3}$ x-ray production cross sections using light ions. However, discrepancies exist between the measured data and the calculations for heavier ions at higher energies. A coupled-state calculation based on the vacancy sharing picture was used by Sarkadi and Mukoyama [9,10] to investigate the *L*-subshell ionization using low-energy heavy-ion collisions. For the heavier projectiles ($Z_1 > 2$) and at the medium energy (>2 MeV/amu) range, few data sets [11–15] are available in the literature and our understanding and knowledge of *L*-subshell ionization is not very satisfactory in the case of heavy-ion collisions. In most of these studies, the x-ray production cross sections are measured and the subshell ionization cross sections are not derived. The ionization cross sections provide an important input for the theory since the calculations generally give the ionization cross sections of different subshells directly, whereas the x-ray cross sections are useful to compare the results of another experiment directly.

Additionally, the derivation of the ionization cross sections from the measured x-ray line intensities (e.g., $L\alpha$, $L\beta$, $L\gamma$) is quite an involved procedure and there are different methods proposed in the literature [16]. It should be stressed here that the ionization cross sections obtained from different methods do show deviations from each other that often amount to several times the quoted errors [11]. This is particularly true for heavy-ion-induced *L*-subshell ionization measurements where the simultaneous creation of vacancies in the higher shells leads to the emission of unresolved satellite lines and thus contributes to the additional broadening of the observed x-ray lines, besides causing changes in the atomic parameters. We have therefore examined the existing methods of converting the x-ray production cross sections to the ionization cross sections for the *L* subshells of Yb, Au, and Bi induced by F ions. These measurements are generally limited to the high-*Z* targets ($Z \geqslant 70$) for which the *L* x-ray lines can be resolved with the help of the Si(Li) x-ray detectors having a resolution of 150–160 eV at 5.9 keV. However,

as will be shown, a meaningful comparison with the theory can only be done provided the multiple vacancies in the outer shells are small.

In the present paper, we are reporting the *L*-subshell ionization cross sections of Yb, Au, and Bi induced by 60–100-MeV F ions. For these collision systems, the ratio of the projectile velocity (v_p) to the orbital velocity of the *L*-shell electrons (v_e) lies between 0.32 and 0.56 (i.e., <1), which represents an adiabatic collision. The PWBA method cannot be applied to describe such low-velocity collisions in which the initial and final states of the active electron are highly distorted by the heavy-ion projectiles. The binding energy of the active electron is drastically increased (as in the limit of united atom) and the projectile goes through a large Coulomb deflection. These effects are incorporated in the ECPSSR model in the form of corrective terms. Therefore the present studies can provide a stringent test for the theory.

II. EXPERIMENTAL DETAILS

Details of the experimental arrangement are discussed in our earlier paper [17] and only a brief description is given here. The experiment was performed with the 14-MV BARC-TIFR Pelletron accelerator at Mumbai. Ions of F^{5+} (60 MeV), F^{6+} (70 MeV), and F^{7+} (83 and 98 MeV) were used for the measurement. The mass and energy analyzed projectile ions were made to fall on thin targets of Bi, Au, and Yb on a carbon backing. To minimize the electron transfer (such as the *L* subshell of the target to the projectile *K*-shell transfer) contribution in the L-shell x-ray productions, targets of small thickness and projectiles with no initial *K* vacancy (see above) are used. Typical thicknesses of the targets were 10 μg/cm^2 for Bi, 5 μg/cm^2 for Au, and 12 μg/cm^2 for Yb. The carbon backing thickness was 10 μg/cm^2. The single collision condition was verified by studying a few targets with different thicknesses. The thickness of the thinnest target used was 5 μg/cm^2 in the case of Yb and Au. It may be mentioned that, in general, thicker ($\geqslant$20 μg/cm^2) targets have been used in most of the previous measurements on the *L* x-ray cross sections (see the reference list) except a few works [15,13]. Therefore, the present investigation gives results on the subshell ionization cross sections using a thinner target compared to several other previous studies. Nevertheless, a small contribution in the target *L* x ray could arise due to *L*-*K* electron transfer inside the target, which was estimated by studying the x-ray yields from the thinnest target as a function of the charge states, i.e., with projectiles having zero and one *K*-shell vacancy. Any contribution due to *L*-*K* transfer will clearly show up in the case of collisions with the H-like ions. The thickness dependences of the *K* x-ray yields for different charge states are available in the literature (see an excellent review by Gray in Ref. [18]). The thickness dependences of the *L* x-ray cross sections have been checked on Yb and Au targets using projectiles (O and F ions) with zero vacancies in the *K* shell [19]. From these studies it was estimated that the correction due to the electron transfer from the *L* shell could be about 10–15 % in the case of Yb, which will increase the systematic errors in our studies. For the Au target, this correction was $<$10% and for Bi it would be negligible as expected on the basis of binding-energy matching conditions.

The targets were mounted at 90° to the beam direction on a rotatable multiple target holder assembly in an electrically isolated chamber [20]. The vacuum inside the chamber during the experiment was $\sim 10^{-6}$ torr.

The x rays emitted from the target were detected by two Si(Li) detectors with a 25-μm-thick Be window and having 160-eV resolution at 5.9 keV. The intrinsic efficiency of the detector was measured using standard radioactive sources and the PIXE (proton-induced x-ray-emission) technique [21]. The detectors were mounted outside the chamber at angles of 135° and 45° with respect to the beam direction. The thicknesses of the targets were obtained, during the measurement, by counting the Rutherford scattered particles at 145° to the beam direction using a Si surface barrier detector. Additional mylar absorbers were used in front of the Si(Li) detectors in order to reduce the large count rate arising from the target *M* x rays in the low-energy part of the spectrum (below 3.5 keV). The absorption of the target *L* x rays (above 7 keV) in the mylar foils was small and taken into account in the analysis. The total count rate under the x-ray spectrum was kept well below 1000 counts/s for Au and Bi and was about 1500 counts/s for the Yb target. To obtain the *L* x-ray production cross sections from the measured x-ray yields, the normalization for the total number of projectiles and target thickness was achieved by simultaneously measuring the elastically scattered charged particles. The beam current was also measured from the entire chamber.

III. DATA ANALYSIS

Typical *L* x-ray spectra of Bi, Au, and Yb are shown in Fig. 1 for 70-MeV F bombardment. As is clear from the spectrum, at least seven different *L* x-ray lines are resolvable and the separation between different peaks increases with higher *Z* targets.

The peak areas in the x-ray spectra were estimated using a multi-Gaussian least-squares-fitting program with the possibility of choosing variable widths of the lines and background subtraction. From the measured x-ray yields, the x-ray production cross sections were estimated using the following relation:

$$\sigma_i^x = \frac{4\pi I_x \sigma_R(\theta) \Delta\Omega_p}{\epsilon I_R \Delta\Omega_x}, \tag{1}$$

where σ_i^x is the x-ray production cross section of the ith line of the *L* spectrum, I_x is the measured x-ray count under the ith line, $\sigma_R(\theta)$ is the differential Rutherford scattering cross section, and I_R is the Rutherford scattered particle count from the target measured by the surface barrier detector. The quantities $\Delta\Omega_x$ and $\Delta\Omega_p$ are the solid angles subtended by the Si(Li) and the surface barrier detectors, respectively. The efficiency of the Si(Li) detector is represented by ϵ, which includes the correction factor due to the absorption of the x rays in the Mylar window. Equation (1) was used to calculate the x-ray production cross section only at lower energies,

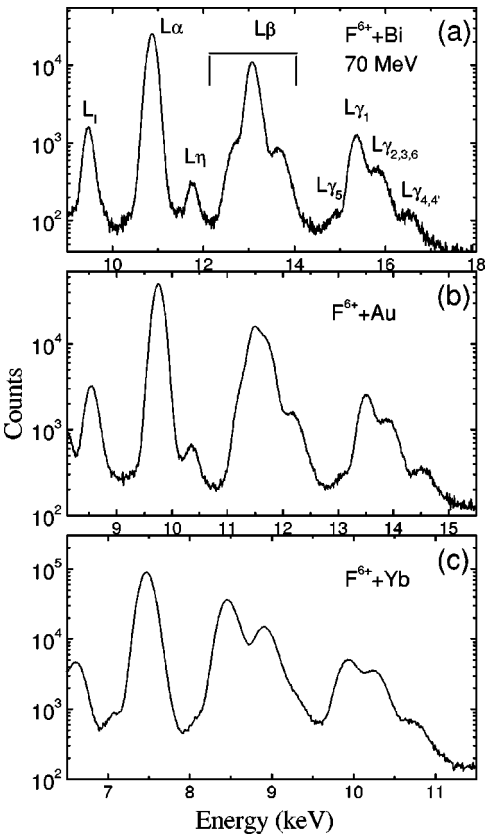

FIG. 1. Typical x-ray spectra obtained with 120-MeV F^{6+} projectiles colliding on the Bi, Au, and Yb targets as indicated in the figures.

i.e., below the Coulomb barrier, above which the beam current normalization was used along with the known target thickness.

The x-ray production cross sections for the most commonly resolved $L\alpha$, $L\beta$, and $L\gamma$ series peaks are then related to the three subshell ionization cross sections σ_i^I $(i=1,2,3)$ and the various atomic parameters in the following ways:

$$\sigma_\alpha^x=[\sigma_1^I(f_{12}f_{23}+f_{13})+\sigma_2^I f_{23}+\sigma_3^I]\omega_3 S_{\alpha 3}, \tag{2}$$

$$\sigma_\beta^x=\sigma_1^I[\omega_1 S_{\beta 1}+\omega_2 f_{12}S_{\beta 2}+\omega_3(f_{13}+f_{12}f_{23})S_{\beta 3}] + \sigma_2^I(\omega_2 S_{\beta 2}+\omega_3 f_{23}S_{\beta 3})+\sigma_3^I\omega_3 S_{\beta 3}, \tag{3}$$

$$\sigma_\gamma^x=\sigma_1^I(\omega_1 S_{\gamma 1}+\omega_2 f_{12}S_{\gamma 2})+\sigma_2^I\omega_2 S_{\gamma 2}, \tag{4}$$

$$\sigma_{\gamma 1}^x=\sigma_1^I\omega_2 f_{12}S_{\gamma 1,2}+\sigma_2^I\omega_2 S_{\gamma 1,2}, \tag{5}$$

$$\sigma_{\gamma 23}^x=\sigma_1^I\omega_1 S_{\gamma 23,1}, \tag{6}$$

$$\sigma_{\gamma 44'}^x=\sigma_1^I\omega_1 S_{\gamma 44',1}, \tag{7}$$

where S_{pi} is the fraction of the radiative transition to the ith subshell associated with the L_p peak [e.g., $S_{\alpha 3}=(\Gamma_{\alpha 1}+\Gamma_{\alpha 2})/\Gamma_3$, where Γ's are the radiative widths], and ω_i is the fluorescence yield of the ith subshell. Equations (2)–(7) link the experimentally measured line intensities to the three unknown subshell ionization cross sections σ_i^I $(i=1,2,3)$. Several combinations of these seven equations can be used to solve for the experimentally measured ionization cross sections. We therefore have a choice of a particular set of peaks, which may be used to deduce the ionization cross sections. Different sets of equations can give rise to a large spread in the final results and may account for some of the discrepancies, which often amount to several times the quoted errors [11]. This aspect was studied earlier for light projectiles such as He [16] where the effect of multiple ionization is not important.

TABLE I. Some of the atomic parameters used in the derivation of the subshell ionization cross sections.

Element	ω_1	ω_2	ω_3	f_{12}	f_{13}	f_{23}	f_1(total)
Bi	0.117	0.387	0.373	0.110	0.580	0.113	0.702
Au	0.107	0.334	0.320	0.140	0.530	0.120	0.687
Yb	0.112	0.222	0.210	0.190	0.290	0.238	0.506

Some of the groups [22] have used an iterative method to get the ionization cross sections from x-ray production cross sections of different x-ray lines. However, four more commonly used approaches (exact solution) will be discussed here. We have used the fluorescence yields and Coster-Kronig transition rates from Ref. [23], shown in Table I and the radiative widths are taken from Ref. [24].

(i) Method 1 or the $\alpha\beta\gamma_{\text{total}}$ method. Most of the L x-ray spectrum is split into three groups, namely $L\alpha$, $L\beta$, and $L\gamma$ regions. Equations (2)–(4) are used to solve for ionization cross sections. Since all the major L lines are used in this technique, statistical counting errors and background subtraction problems are minimal here. One main disadvantage of this method is the usage of the maximum number of atomic parameters, which are known for single vacancy atoms only. For heavy-ion-induced collision, multiple ionization causes additional complications since the atomic parameters are changed, which ultimately affects the cross-section values. Ionization cross-section calculation using this method sometime gives even negative value which are, however, not possible.

(ii) Method 2 or the $\alpha\gamma_1\gamma_{44'}$ method. In this approach, the intensity of the $L\gamma_1$, $L\gamma_{44'}$, and $L\alpha$ peaks is needed and Eqs. (2), (5), and (7) are used. Compared to method 1, here the number of atomic parameters used is much lower, but the main disadvantage is that the total counts under the $L\gamma_{44'}$ peak are much smaller than those in the $L\alpha$ or $L\gamma_1$ peaks, and thus the method suffers from poor statistics. Moreover, the peak is situated at the falling portion of the $L\gamma_{236}$ peak. Accurate background subtraction for such a small peak introduces a large error in the determination of $\sigma_{\gamma_{44'}}^x$ and hence σ_1^I. This situation is more aggravated because of larger widths as a result of multiple ionization. However, this is an acceptable method provided good statistics under the $L\gamma_{44'}$ line is achieved, and in fact it has been used by several authors.

(iii) Method 3 or the $\alpha\gamma_1\gamma_{\text{total}}$ method: In this approach,

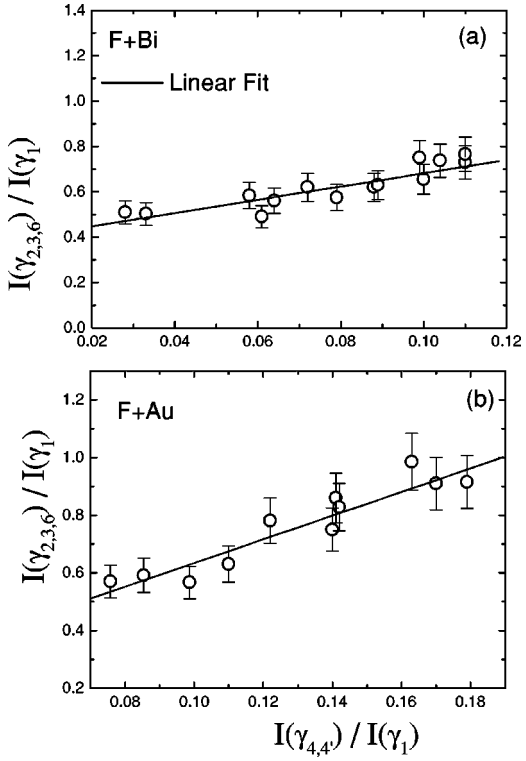

FIG. 2. The measured intensity ratio $I(\gamma_{2,3,6})/I(\gamma_1)$ for Bi and Au targets as a function of the ratio $I(\gamma_{4,4'})/I(\gamma_1)$. The different points are derived at different beam energies or charge states. The fitted straight lines through the data points are also shown.

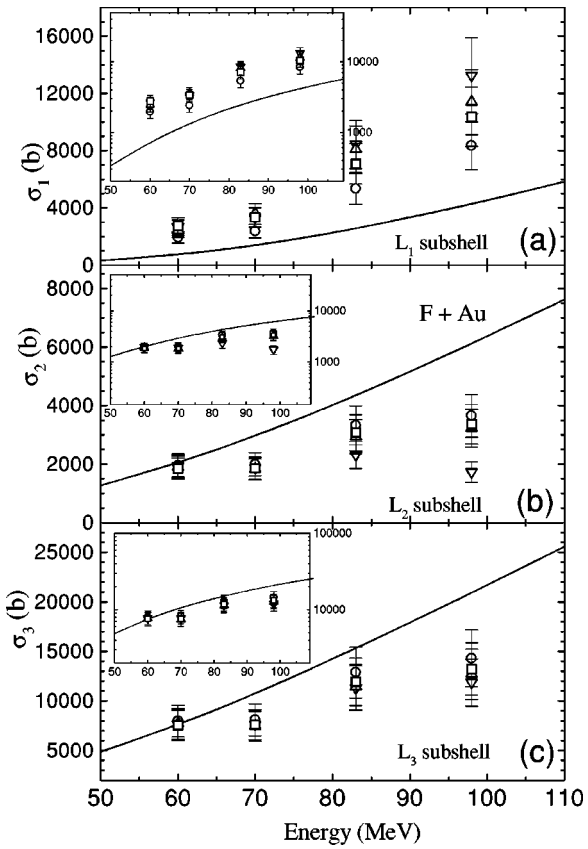

FIG. 3. The deduced values for the (a) L_1, (b) L_2, and (c) L_3 subshell ionization cross sections for Au as a function of the beam energy. The different symbols represent the cross sections obtained using different methods (see text). The inverted triangles, triangles, squares, and circles represent the data obtained using method 1, 2, 3, and 4, respectively. The lines shown in the figures correspond to the ECPSSR calculations. The inset shows the same data and the calculations in a logarithmic scale.

the intensities of the $L\gamma_1$, the total $L\gamma$, and the $L\alpha$ peaks are needed and Eqs. (2), (4), and (5) are used. Compared to method 1, the atomic parameters used here are much less in number. Since γ_1 is the strongest line among the γ structure, there is also no problem of Gaussian peak fitting or background subtraction. But compared to method 2, the number of atomic parameters used here is higher.

(iv) Method 4 or the $\alpha\gamma_1\gamma_{23}$ method. The intensities of $L\gamma_1$, $L\gamma_{23}$, and $L\alpha$ peaks are needed and Eqs. (2), (5) and (6) are used in this method. For the heavy-ion-induced x-ray emission, only $L\gamma_1$ and $L\gamma_{236}$ lines can be clearly fitted with Gaussian peaks (see Fig. 1). Now the $L\gamma_{23}$ line originates due to a vacancy in the L_1 subshell, while $L\gamma_6$ is from the L_2 subshell. So to obtain the ionization cross section one has to subtract the contribution from the $L\gamma_6$ line. We have followed Datz's prescription [25] to estimate the contribution of the $L\gamma_6$ intensity in the $L\gamma_{236}$ as they are unresolvable. If the transition probability ratio $\Gamma\gamma_6/\Gamma\gamma_1$ is known, the γ_6 contribution to the intensity can be subtracted from the area of γ_{236} complex. A plot of $I(\gamma_{236})/I(\gamma_1)$ derived at different energies versus $I(\gamma_{44'})/I(\gamma_1)$ was found to be linear and the projected intercept on the Y axis at $I(\gamma_{44'})/I(\gamma_1)=0$ provides us with the required ratio of transition probabilities, i.e., $\Gamma\gamma_6/\Gamma\gamma_1$. Such plots for Bi and Au are shown in Fig. 2. The $\Gamma\gamma_6/\Gamma\gamma_1$ values for Bi and Au are 0.39 and 0.22, respectively. These are quite large compared to the theoretical values, e.g., for Bi and Au they are 0.144 and 0.106, respectively. For the case of Yb, the $L\gamma_6$ line should not come into the picture because of the absence of the O_{IV} electron in its shell and no correction is necessary for the $L\gamma_6$ line. However, we have tried to calculate the $\Gamma_{\gamma 6}/\Gamma_{\gamma 1}$ value, for Yb from the experiment and it shows quite a high value which is not acceptable in a real sense.

This method also uses fewer atomic parameters, as does method 2, and since the lines used in this method are strong enough, the peak fitting and background subtraction pose no problem. One disadvantage of this method is the calculation of the $\Gamma\gamma_6/\Gamma\gamma_1$ ratio, which is extremely sensitive to the areas under the $\gamma_{44'}$ and γ_{236} lines. For the heavy-ion-induced x-ray emission case in which the lines are broadened due to multiple ionization, one has to be particularly careful about the determination of the intensity of the $\gamma_{44'}$ line. An error in area determination of this line (as well as γ_{236} line) ultimately affects the ratio of $\Gamma_{\gamma 6}/\Gamma_{\gamma 1}$ and hence the L_1 ionization cross section.

Here we have derived the subshell ionization cross sections using all the methods, and the results are shown in Figs. 3, 4, and 5. It may be seen from these figures that method 1 always differs from the other three methods, and in our case since we have good statistics in the $\gamma_{44'}$ line the results obtained from methods 2 and 4 are not much different.

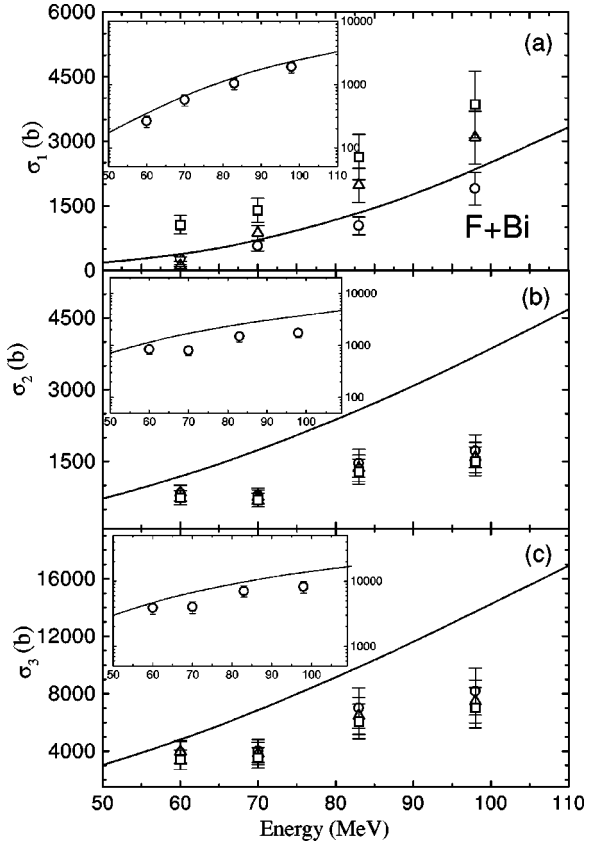

FIG. 4. Same as in Fig. 3 except for Bi.

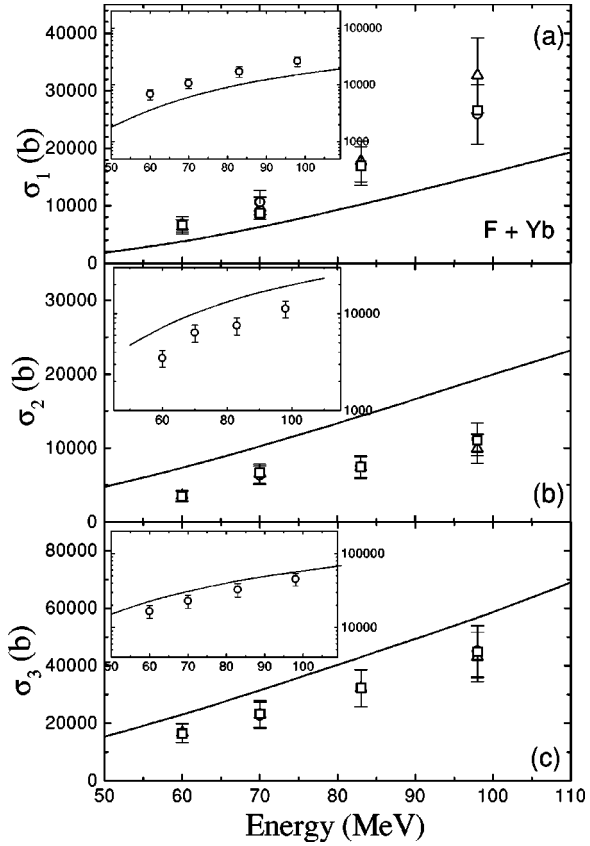

FIG. 5. Same as in Fig. 3 except for Yb.

It may be noted that the Ll, $L\eta$, and $L\beta$ lines are not used at all in the derivation of the subshell ionization cross sections. As a cross check on the different methods used, we have derived the x-ray production cross sections for the Ll, $L\eta$, and $L\beta$ using the measured subshell ionization cross sections and then compared them with the measured production cross sections of these three lines. The comparison is displayed in Figs. 6(a), 6(b), and 6(c) as a ratio of the measured to the derived cross sections for the Ll, $L\eta$, and $L\beta$ lines for the Au target. It can be seen that in the case of $L\beta$, the measured cross sections are in good agreement with the derived ones within about 5–10 % (i.e., ratio 1.05–1.1) for all the methods [Fig. 6(c)]. However, all of them are within each other's error bars and they are not at all sensitive to the ionization cross section used for calculating the x-ray production cross section of different lines. For the Ll line [Fig. 6(a)], the experimental and calculated cross sections are within 20% of each other and for the $L\eta$ [Fig. 6(b)] line the agreement is worse, though all the methods give identical results.

IV. RESULTS AND DISCUSSIONS

It is clear from Fig. 3 that, particularly for the $L1$ subshell, method 1 shows higher values compared to the other methods and the difference increases with increasing energies. The reason for this may be the use of the maximum number of atomic parameters in method 1. It is well established (see Ref. [26] and references therein) that in heavy-ion collision the probability of multiple ionization is greater and therefore the atomic parameters would change, which will further affect the extraction of the subshell ionization cross section from x-ray production. It may be seen that there are

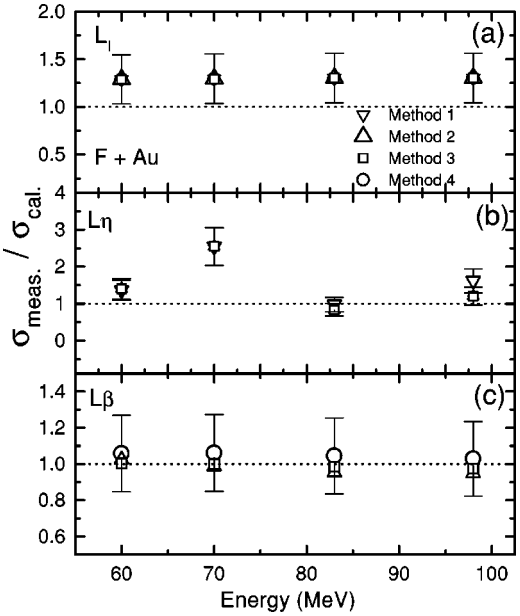

FIG. 6. The ratios of the measured x-ray production cross sections of (a) L_l, (b) L_η, and (c) L_β x rays for Au to those calculated using the subshell ionization cross sections (σ_1, σ_2, and σ_3) derived using four different methods (as indicated in the figure).

TABLE II. The measured x-ray production cross sections of different lines of Bi, Au, and Yb induced by F ions.

Target	Energy	Ll (b)	$L\alpha$ (b)	$L\beta$ (b)	$L\gamma_{15}$ (b)	$L\gamma_{23}$ (b)	$L\gamma_{44'}$ (b)
Bi	60	63	1180	661	58	6	0.52
	70	65	1271	731	58	14	4.15
	83	126	2230	1300	107	24	9.44
	98	134	2713	1646	130	45	14.72
Au	60	153	2336	1370	125	42	9
	70	160	2431	1463	131	51	14
	83	270	4081	2586	229	115	31
	98	322	4868	3201	271	179	44
Yb	60	143	3242	2164	169	148	18
	70	238	4568	3146	296	230	28
	83	373	6565	4777	381	367	51
	98	385	9300	3016	573	562	94

some differences ($\Delta\sigma$) among the cross sections derived using different methods. Although the absolute values of the differences change with the beam energy, the fractional differences (i.e., $\Delta\sigma/\langle\sigma\rangle$) in these values remain almost the same for all energies, which is obvious from the logarithmic plots in the insets in Figs. 3(a), 3(b), and 3(c). It is found from Fig. 3 that the observed cross sections for Au are σ_{L1}(method 1) $>\sigma_{L1}$(method 2) $>\sigma_{L1}$(method 3) $>\sigma_{L1}$(method 4). In the case of $L2$, method 1 shows the lowest cross section among all the methods and it shows the largest cross sections for L_1. The largest deviation for method 1 is due to using the maximum number of atomic parameters. However, for the case of $L3$, since all four methods use the $L\alpha$ line, the cross sections calculated by all the methods are almost the same and within the error bars. Methods 2, 3, and 4 give the results within each other's error bar, especially for L_2 and L_3 subshells. In the case of Bi, method 4 gives the lowest cross sections of the L_1 subshell as in the case of Au and all three methods produce the same results for L_2 and L_3. A similar trend is also observed for Yb, i.e., all three methods produce the same results. Note that method 1 (i.e., the $\alpha\beta\gamma_{\text{total}}$ method) is not used for Yb and Bi since this method gave negative results.

It may be emphasized that the measured x-ray production cross sections are independent of any model, unlike the deduced values of the ionization cross sections, and thus can be directly compared with the other available data on x-ray production cross sections. The x-ray production cross sections of different lines are tabulated in Table II. In order to test the validity of the theoretical models, which provide the ionization cross sections only, we have used the ionization cross-section values obtained by method 4, which are tabulated in Table III. Experimental data for L_1 cross sections fall much above, i.e., a factor of about 2 higher than the ECPSSR calculations for the Au [Fig. 3(a)] and Yb [Fig. 4(a)] targets and the deviation remains the same (approximately) over the present energy range [see the insets in Figs. 3(a) and Figs. 4(a), which show that the ECPSSR and the data are almost parallel]. The deviation from the ECPSSR can also be seen more clearly in Figs. 7(a)–7(c), in which the ratios of the experimental data to the ECPSSR calculations are plotted. For the Bi target, the calculation reproduces the L_1-ionization cross sections much better than those for Au and Yb. However, the calculations still fall about 20% below the data [see Figs. 4(a) and 7(a)]. In the case of L_2 and L_3 (see Figs. 3–5), the theory generally underestimates the experimental data for all three targets and the deviations remain approximately similar over the energy range. These can be seen also from Figs. 7(b) and 7(c).

One interesting observation is that the L_1-ionization cross section is higher than the L_2-ionization cross sections for the

TABLE III. L_1, L_2, and L_3 subshell ionization cross sections of Bi, Au, and Yb induced by F ions. The errors in the data points are about 20–25 %. In the case of a Yb target, a small contribution of L-K electron capture is included and therefore the ionization cross sections would be reduced by about 10–15 %.

Target	Energy (MeV)	σ_1 (b)	σ_2 (b)	σ_3 (b)
Bi	60	263	833	3870
	70	570	790	4010
	83	1036	1466	7005
	98	1894	1720	8154
Au	60	1940	1961	7972
	70	2380	1994	8104
	83	5338	3324	12873
	98	8351	3653	14309
Yb	60	6799	3466	16478
	70	10601	6318	22696
	83	16949	7511	32294
	98	25905	11198	45071

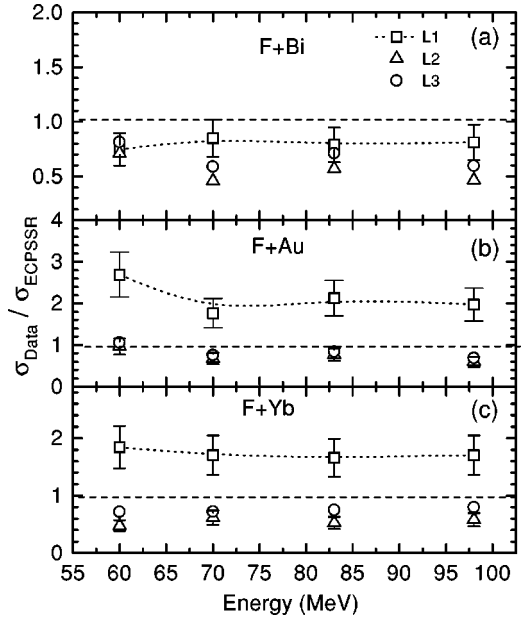

FIG. 7. The ratios of the measured subshell ionization cross sections (σ_{data}) to the ECPSSR predictions (σ_{ECPSSR}) for Yb, Au, and Bi. The squares, triangles, and circles represent the ratios for the L_1, L_2, and L_3 subshells, respectively. The dotted lines through the L_1 data points are only to guide the eyes. The dashed lines represent the ratio 1.0.

Au and Yb targets. The binding energy (absolute value) of L_1 is higher than that of L_2 and hence one would expect σ_1 to be less than σ_2. Similar observations were also made in the past in this energy range [11–13]. However, for the case of Bi the L_1 and L_2 subshell ionization cross sections show the right trend, i.e., $\sigma_1 < \sigma_2$.

These observations are shown in Fig. 8, where we have plotted the cross-section ratios, i.e., σ_1/σ_2 and σ_2/σ_3. Measurement of relative subshell cross sections is not affected by the uncertainties of the absolute normalization but is still sensitive to the various aspects of the ionization mechanism. We have compared these ratios with the ECPSSR theory. It is seen from Fig. 8 that for σ_1/σ_2, the theory does not match well with the experimental values. The measured values are about two to three times higher than the theoretical predictions, especially for Au and Yb, while for Bi the agreement is not as bad. The reason for this discrepancy lies in the extraction of ionization cross sections from the experimentally measured x-ray production cross sections for different lines. Heavy-ion impact results in multiple ionization in outer shells, and due to this the atomic parameters that are used in the data analysis (applicable for singly ionized atoms) may differ considerably. For example, in the case of Yb, Au, and Bi targets we observed an average energy shift of 46 eV, 25 eV, and 17 eV (see Table IV), respectively, for the $L\alpha$ line and the shifts were found to be almost independent of energy in the present energy range. This indicates the simultaneous creation of more than one *M* vacancy and several *N* vacancies in the case of Au [27,28] during collision, and the effect of multiple ionization will remain almost the same over the present energy range. The higher energy shift of the $L\alpha$ line represents a larger degree of multiple ionization in the outer shell simultaneous with the *L* vacancy. In the present velocity range, the *M* shell ionization probability is either maximum or near maximum since v_p/v_e^M varies between 0.7 and 1.5 (0.95–1.5 for Yb, 0.78–1.0 for Au, and 0.73–0.93 for Bi using average binding energies of *M* subshells), whereas the *N*-shell ionization probability decreases with beam energy. It can be seen that the energy shifts of $L\alpha$, $L\eta$, and Ll (Table IV) clearly reflect the vacancies present in the *M* shell. The energy shifts are not so sensitive to the vacancies in the outermost shells such as *N* and *O*, rather they are more sensitive to the holes present in the *M* shell.

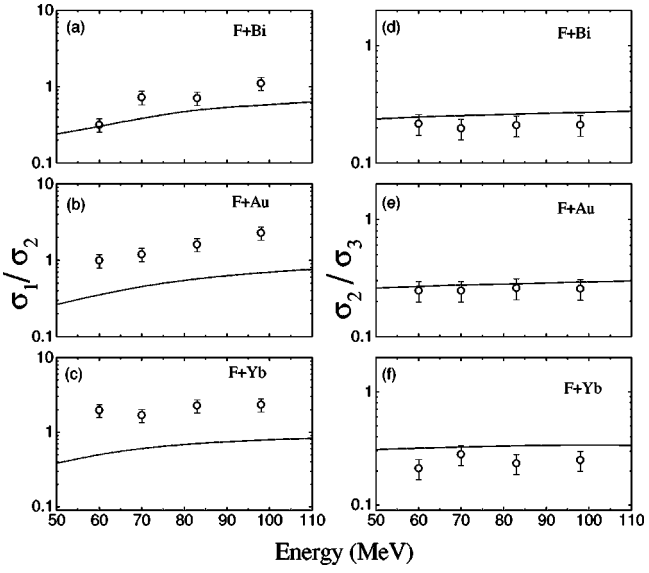

FIG. 8. The ratios of different subshell ionization cross sections, i.e., σ_1/σ_2 and σ_2/σ_3 for Bi, Au, and Yb as a function of beam energy. The ECPSSR calculations are shown as solid lines.

TABLE IV. The energy shifts of $L\alpha$ (ΔE_α), $L\eta$ (ΔE_η), and Ll (ΔE_l) lines. The errors are about ± 5–10 eV.

Target	Energy (MeV)	ΔE_α (eV)	ΔE_η (eV)	ΔE_l (eV)
Bi	60	15	29	36
	70	23	29	36
	83	15	23	36
	98	15	29	36
Au	60	33	46	35
	70	23	46	35
	83	23	46	35
	98	23	46	35
Yb	60	46		
	70	46		
	83	46		
	98	46		

However, the effect of *M*-shell vacancies will be particularly large for the L_1 subshell fluorescence yield ω_1. Accord-

ing to the calculations of Scofield [29] and Chen *et al.* [23], about half of the L_1 decay in the singly ionized atoms occurs via the $L_1-L_3M_{4,5}$ Coster-Kronig channel (for Au and Bi it is ~ 0.40). As may be seen from Table I (and Fig. 6 of Ref. [29]), the Coster-Kronig (CK) transition rate f_1 (for L_1) is much higher than ω_1. In the case of multiple ionization in the M shell, the CK channel may be blocked and as a consequence the CK rate f_{13} may be drastically reduced and the fluorescence yield ω_1 increases roughly by a factor of 2 [11]. It is also clear from Fig. 8 that the ratio σ_1/σ_2 for Bi, since the probability of multiple ionization is lower, shows better agreement with theory and the deviation increases from Au to Yb.

In contrast, the value of ω_2 is much higher (see Table I) than the Coster-Kronig transition rate f_{23} and so the change of f_{23} will not have much of an effect on the L_2 subshell fluorescence yield (Fig. 8 of Ref. [30]). The L_3 subshell fluorescence yield ω_3 is least affected because of the absence of Coster-Kronig transitions. So the experimental data on the ratio of the cross sections of the L_2 and L_3 subshells, i.e., σ_2/σ_3 are more appropriate to test the theory. Figure 8 shows that the measured ratios are in good agreement with the theory. Thus, it is obvious that it is not proper to test the theory with the measured L_1 cross sections since the fluorescence yield parameter ω_1 is uncertain by a large amount for heavy-ion impact. On the other hand, the L_3 (and also to some extent the L_2) subshell cross section is most reliable and also the ratio σ_2/σ_3.

From the data and the comparison with the theory it may be possible to estimate the enhancement in the L_1-subshell fluorescence yield. This is based on the assumption that the deviations of the ECPSSR from the data are almost the same for all three subshells since they have almost the same binding energies. The nodal character of the wave function for the L_1 subshell will not affect the energy dependence of the cross sections at the present energy range. In Fig. 7, we have displayed the ratio of the data to the ECPSSR calculations for Yb, Au, and Bi targets. It is clearly seen from Fig. 7(a) that for the Bi target the ratio for all three subshells bunches together, i.e., to between 0.5 and 0.8, whereas in the case of Au and Yb the ratio for L_1 is very large (around 2.0) compared to that for L_2 and L_3. A close look into the ratio for L_1 compared to those for L_2 and L_3 may give an idea of the degree of enhancement in the value of ω_{L1}. In the case of Bi, the average ratio for L_3 is about 0.6 or 0.7 and that for L_1 is 0.8 indicating that an enhancement in ω_{L1} is about 25%. We have assumed that the enhancement in the ω_{L2} and ω_{L3} are quite small, i.e., about 5% based on our calculations using Larkins' statistical principle [31]. In the case of Yb and Au, the ω_{L1} is enhanced by a factor of about 2.5 ± 0.5.

V. CONCLUSION

We have measured the L-subshell ionization cross sections for Yb, Au, and Bi targets for F ions in the intermediate velocity range. Four different methods are used to derive the ionization cross sections from the x-ray production cross sections. The merits of the different methods are discussed. The multiple ionization of the higher shells of the target atoms has a considerable influence on the atomic parameters and thus prevents a reliable extraction of the L_1-ionization cross section from the experimentally observed line intensities, especially for Au, Yb, and lighter targets. The ECPSSR calculations are found to underestimate the L_2 and L_3 cross sections for all three targets. The L_1 cross sections are apparently much higher for Yb and Au due to a large enhancement in the L_1-fluorescence yield and a quantitative estimation is also provided for such enhancements. Accordingly, the ratios of the derived cross sections for L_1 and L_2 are found to be much larger than 1.0 for Yb and Au, contrary to the theoretical predictions, whereas the ratio is less than 1.0 for Bi, as expected. The ECPSSR gives a better agreement with the measured L_1-subshell ionization cross sections for Bi, although the theory falls slightly below the data.

It is shown that the subshell ionization cross sections for L_2, L_3, and their ratios are more suitable quantities to compare with theory instead of the data for L_1 subshell for targets such as Yb and Au. It may be concluded that the Bi and higher Z targets are better suited for the investigation of heavy-ion-induced L-subshell ionization using the experimental conditions and measurement techniques similar to the present investigation.

ACKNOWLEDGMENTS

The authors thank K.V. Thulasiram for his assistance in the experiments and the machine staff for the smooth operation of the accelerator.

[1] W. Brandt, R. Laubert, and L. Sellin, Phys. Rev. **151**, 56 (1966).
[2] F. D. McDaniel, A. Toten, R. S. Petersen, J. L. Duggan, S. R. Wilton, J. D. Gressett, P. D. Miller, and G. Lapicki, Phys. Rev. A **19**, 1517 (1979).
[3] E. Merzbacher and H. W. Lewis, in *Handbuch der Physik*, edited by S. Flugge (Springer-Verlag, Berlin, 1958), p. 166.
[4] J. Bang and J. M. Hansteen, K. Dan. Vidensk. Selsk. Mat. Fys. Medd. **31**, 13 (1959).
[5] W. Brandt and G. Lapicki, Phys. Rev. A **23**, 1717 (1981).
[6] D. Trautmann and G. Baur, Nucl. Instrum. Methods Phys. Res. B **40/41**, 345 (1989).
[7] M. H. Martir, A. L. Ford, J. F. Reading, and R. L. Becker, J. Phys. B **15**, 2405 (1982).
[8] R. Singhal, N. B. Malhi, and T. J. Gray, J. Phys. B **25**, 2055 (1992).
[9] L. Sarkadi and T. Mukoyama, Phys. Rev. A **42**, 3878 (1991).
[10] L. Sarkadi, T. Mukoyama, and Z. Smit, J. Phys. B **29**, 2253 (1996).
[11] W. Jitschin, R. Hippler, K. Finck, R. Schuch, and H. O. Lutz, J. Phys. B **16**, 4405 (1983), and references therein.
[12] H. C. Padhi, B. B. Dahl, V. Nanal, K. G. Prasad, P. N. Tandon,

and D. Trautmann, Phys. Rev. A **54**, 3014 (1996).
[13] B. B. Dhal, A. K. Saha, Lokesh C. Tribadi, K. G. Prasad, and P. N. Tandon, J. Phys. B **31**, L807 (1998).
[14] N. B. Mahli and T. J. Gray, Phys. Rev. A **44**, 7199 (1991); T. J. Gray and N. B. Mahli, J. Phys. B **29**, 1331 (1996).
[15] M. C. Andrews, F. D. McDaniel, J. L. Duggan, P. D. Miller, P. L. Pepmiller, H. F. Krause, T. M. Rosseel, L. A. Rayburn, R. Mehta, and G. Lapicki, Phys. Rev. A **36**, 3699 (1987).
[16] D. D. Cohen, J. Phys. B **17**, 3913 (1984).
[17] L. C. Tribedi, K. G. Prasad, P. N. Tandon, Z. Chen, and C. D. Lin, Phys. Rev. A **49**, 1015 (1994).
[18] T. J. Gray, in *Methods of Experimental Physics*, edited by P. Richard (Academic Press, New York, 1980), Vol. 17, p. 193, and references therein.
[19] A. K. Saha, L. C. Tribedi, B. B. Dhal, and P. N. Tandon (unpublished).
[20] L. C. Tribedi, S. D. Narvekar, R. G. Pillay, and P. N. Tandon, Pramana **39**, 661 (1992).
[21] L. C. Tribedi and P. N. Tandon, Nucl. Instrum. Methods Phys. Res. B **62**, 178 (1992).
[22] C. N. Chang, J. F. Morgan, and S. L. Blatt, Phys. Rev. A **11**, 607 (1975).
[23] M. H. Chen, B. Crasemann, and H. Mark, Phys. Rev. A **24**, 177 (1981).
[24] J. L. Campbell and J.-X. Wang, At. Data Nucl. Data Tables **43**, 281 (1989).
[25] S. Datz, J. L. Duggan, L. C. Feldman, E. Laegsgaard, and J. U. Andersen, Phys. Rev. A **9**, 192 (1974).
[26] D. Banaśet *et al.*, Nucl. Instrum. Methods Phys. Res. B **154**, 247 (1999).
[27] G. Bissinger, P. H. Nettles, S. M. Shaforth, and A. W. Waltner, Phys. Rev. A **10**, 1932 (1974).
[28] P. H. Mokler, Phys. Rev. Lett. **26**, 811 (1971).
[29] J. H. Scofield, At. Data Nucl. Data Tables **14**, 121 (1974).
[30] M. O. Krause, J. Phys. Chem. Ref. Data **8**, 307 (1979).
[31] F. P. Larkins, J. Phys. B **4**, L29 (1971).